OPTIMIZED REDUCED GRAPHENE OXIDE-TiO_2 NANOCOMPOSITE WITH CO-SENSITIZATION STRATEGY: ENHANCING DYE-SENSITIZED SOLAR CELL PERFORMANCE THROUGH ADVANCED INTERFACIAL ENGINEERING AND CHARGE TRANSPORT OPTIMIZATION

Gwani, Muhammad Mustapha[1]; Gambo, Muhammad Hassan[2]; Gimba, Ahmed Mohammed[3]

[1]*Department of Physics, Federal University Lokoja, Kogi State, Nigeria* • [2]*Department of Physics, Nigerian Defence Academy, Kaduna State, Nigeria* • [3]*Department of Physics, Nigerian Army University Biu, Borno State, Nigeria*

gwani.mustapha@fulokoja.edu.ng

Cite this article as: Gwani, M. M., Gambo, M. H., & Gimba, A. M. (2026). Optimized reduced graphene oxide-TiO_2 nanocomposite with co-sensitization strategy: Enhancing dye-sensitized solar cell performance through advanced interfacial engineering and charge transport optimization. Journal of Interdisciplinary Postgraduate Research, 1(2), 228–234.

Abstract

This study reports a systematic optimization of reduced graphene oxide (rGO) modified TiO_2 photoelectrodes for dye-sensitized solar cells (DSCs), addressing a critical limitation in which device efficiencies had remained below 0.15 percent. Through a comprehensive parametric investigation of rGO loading concentration (0.5 to 10 mg/mL), synthesis temperature (200 to 400 degrees Celsius), and a co-sensitization strategy combining the natural dye Delonix regia with the N719 ruthenium complex, substantial performance gains were realised. Electrochemical impedance spectroscopy revealed that an optimal rGO loading of 3 mg/mL reduced the charge transfer resistance at the photoelectrode and electrolyte interface by sixty seven percent relative to bare TiO_2, while incident photon-to-current conversion efficiency measurements demonstrated a broadened spectral response extending to 800 nm with a peak quantum efficiency of seventy eight percent at 530 nm. The optimized cell, combining a 3 mg/mL rGO-TiO_2 photoelectrode, one-to-one co-sensitization, and an electrochemically deposited polyaniline counter electrode, exhibited a short-circuit current density of 8.42 mA/cm^2, an open-circuit voltage of 0.71 V, a fill factor of 0.68, and a power conversion efficiency of 4.06 percent under AM 1.5G illumination, a thirty one fold improvement over the prior baseline. Accelerated aging confirmed retention of ninety one percent of the initial efficiency after one thousand hours of continuous illumination. The synergistic interplay of optimized interfacial properties and complementary light absorption establishes a viable route toward cost effective, durable DSCs built on earth abundant materials and partially natural photosensitizers.

Keywords: *dye-sensitized solar cells, reduced graphene oxide, TiO_2 nanocomposite, co-sensitization, natural dyes, interfacial engineering*

1. Introduction

The global imperative for sustainable energy has elevated third generation photovoltaic technologies to prominence as credible alternatives to conventional silicon devices, particularly where affordability and environmental compatibility are decisive (Green et al., 2021; Sharma et al., 2018). Among these technologies, dye-sensitized solar cells have attracted sustained interest since the seminal contribution of O'Regan and Gratzel (1991), offering low cost fabrication, a tolerable efficiency under diffuse illumination, and aesthetic flexibility through colour tunability (Gratzel, 2003). The characteristic architecture, a mesoporous semiconductor photoelectrode sensitized with light absorbing dye molecules, a redox electrolyte that mediates charge transport, and a catalytic counter electrode, spatially separates light absorption from carrier transport and so avoids several constraints intrinsic to conventional cells (Hagfeldt et al., 2010).

Notwithstanding three decades of intensive research and certified efficiencies above fourteen percent achieved with ruthenium sensitizers and elaborate electrolyte chemistry (Kakiage et al., 2015), several obstacles continue to delay widespread commercialisation. The cost and scarcity of ruthenium dyes, the environmental burden of volatile organic electrolytes, and the gradual degradation of platinum counter electrodes in iodide systems remain the most stubborn (Wu et al., 2017; Bella et al., 2015). These difficulties have stimulated work toward wholly sustainable configurations that rely on natural dyes, non-precious catalysts, and earth abundant semiconductors (Calogero et al., 2015; Narayan, 2012).

In an earlier study, Ahmed et al. (2020) integrated an rGO-TiO_2 photoelectrode with a polyaniline counter electrode in a cell sensitized with *Delonix regia* extract, recording a sixty nine percent efficiency gain over unmodified TiO_2 yet an absolute efficiency of only 0.13 percent. That work was limited to current and voltage measurement, employed an unoptimized 10 mg/mL rGO loading, and relied solely on a natural dye whose narrow absorption band restricts light harvesting. The present investigation was designed to remove each of these limitations in turn.

Three deliberate interventions structure the study. First, a parametric series fixed the optimal rGO concentration by varying loading from 0.5 to 10 mg/mL and relating photoelectrode properties to device output. Second, recognising that the narrow spectrum of the natural dye fundamentally caps light harvesting, a co-sensitization strategy paired *Delonix regia* with the well characterised N719 complex so that the complementary absorption bands of the two sensitizers broaden spectral coverage while preserving the economic and ecological merits of partial natural dye use (Ogomi et al., 2014; Chang et al., 2013). Third, advanced characterisation through electrochemical impedance spectroscopy and incident photon-to-current conversion efficiency was applied to resolve interfacial charge transfer, recombination dynamics, and the wavelength resolved quantum efficiency that simpler measurements cannot reveal (Fabregat-Santiago et al., 2011; Wang et al., 2005).

A complementary objective concerned durability. Practical deployment demands sustained output rather than a high initial figure alone, and so the optimized devices were subjected to accelerated aging across one thousand hours of continuous illumination, an aspect entirely absent from the preliminary work yet indispensable for any assessment of real world viability (Hinsch et al., 2001). The counter electrode was likewise refined, with the electropolymerisation of polyaniline tuned to raise catalytic activity toward triiodide reduction while improving adhesion (Hou et al., 2013; Tai et al., 2010). The investigation thus converts an early proof of concept into a mechanistic and quantitative study that clarifies how graphene modification governs electron injection, transport, and recombination, the graphene sheets acting at once as transport highways and as barriers to back electron transfer (Yang et al., 2010; Liang et al., 2011).

2. Materials and Methods

2.1 Materials and Synthesis

Graphene oxide was prepared from natural graphite flake by a modified Hummers method and reduced in situ during the hydrothermal growth of TiO_2. Titanium tetraisopropoxide served as the titanium precursor. Reduced graphene oxide and TiO_2 were combined hydrothermally at concentrations spanning 0.5 to 10 mg/mL, the suspensions being treated at 180 degrees Celsius for twelve hours before calcination. Synthesis temperature was varied from 200 to 400 degrees Celsius to examine its influence on the rGO and TiO_2 interface and the resulting electron transport. The mesoporous photoelectrode was screen printed onto fluorine doped tin oxide glass and sintered through a staged profile that ramped to 500 degrees Celsius, a gradual schedule that prevents cracking while removing organic residues and promoting interparticle contact. A scattering overlayer of 200 nm TiO_2 was added to enhance light harvesting, giving a mesoporous active layer of about ten micrometres and a scattering layer of about four micrometres as measured by profilometry.

2.2 Dye Extraction and Sensitization

Fresh *Delonix regia* flowers were extracted in acidified ethanol at sixty degrees Celsius under reflux in darkness to protect the anthocyanin pigments, then filtered and concentrated under reduced pressure. Three sensitization protocols were compared: exclusive natural dye, exclusive N719, and a sequential co-sensitization in which electrodes were first immersed in diluted *Delonix regia* extract, rinsed and dried, and then immersed in 0.3 mM N719. The co-sensitization ratio was tuned through the dilution factor and immersion times.

2.3 Counter Electrode and Cell Assembly

Polyaniline counter electrodes were grown by potentiodynamic electropolymerisation from an aniline and sulfuric acid bath, the films displaying the emerald green of the conductive emeraldine salt. Platinum counter electrodes were prepared by thermal decomposition of chloroplatinic acid for comparison. Cells were assembled in a sandwich geometry sealed with Surlyn, the iodide and triiodide electrolyte introduced by vacuum backfilling, and the active area defined precisely at 0.25 cm^2. Each configuration was fabricated in triplicate.

2.4 Characterisation and Performance Metrics

Journal of Interdisciplinary Postgraduate Research 2026,Vol. 1 (2) DOI: 10.61955/CMXJYZ

Morphology and microstructure were examined by field emission scanning electron microscopy and transmission electron microscopy. Crystalline phase was resolved by X-ray diffraction with copper K-alpha radiation, and the degree of graphene reduction was assessed by Raman spectroscopy under 532 nm excitation. Surface chemistry was probed by X-ray photoelectron spectroscopy. Current density and voltage characteristics were measured under an AM 1.5G solar simulator calibrated to 100 mW/cm^2, and incident photon-to-current conversion efficiency and electrochemical impedance spectroscopy were recorded to resolve quantum efficiency and interfacial processes. The overall power conversion efficiency follows from the standard definition in Equation 1,

$$\eta = (J_{sc} \times V_{oc} \times FF) / P_{in} \quad (1)$$

where J_{sc} is the short-circuit current density, V_{oc} the open-circuit voltage, FF the fill factor, and P_{in} the incident power density. The fill factor itself is defined in Equation 2 as the ratio of maximum power to the product of the limiting current and voltage,

$$FF = (J_{mp} \times V_{mp}) / (J_{sc} \times V_{oc}) \quad (2)$$

The integrated photocurrent expected from the spectral response is obtained from the incident photon-to-current conversion efficiency through Equation 3,

$$J_{sc} = q \int IPCE(\lambda) \times \Phi(\lambda)\, d\lambda \quad (3)$$

in which $\Phi(\lambda)$ is the AM 1.5G photon flux and q the elementary charge. The electron lifetime that governs recombination is extracted from the impedance response through Equation 4,

$$\tau_n = R_{ct} \times C_{\mu} \quad (4)$$

where R_{ct} is the charge transfer resistance at the photoelectrode and electrolyte interface and C_{μ} the chemical capacitance of the film.

3. Results and Discussion

3.1 Structural and Morphological Characterisation

Figure 1 presents the X-ray diffraction patterns and Raman spectra of bare TiO_2 and the rGO-TiO_2 nanocomposites. The diffraction patterns confirm the anatase phase through the characteristic reflection near 25.3 degrees and the further reflections at 37.8, 48.0, 53.9, and 55.1 degrees, with no extraneous peaks that would signal a secondary phase. The incorporation of rGO produces no measurable shift in peak position, indicating that the graphene sheets decorate the TiO_2 surface without entering the lattice. The Raman spectra resolve the D and G bands of carbon near 1350 and 1580 reciprocal centimetres alongside the anatase modes, and the intensity ratio of the two carbon bands confirms a substantial degree of reduction consistent with conductive graphene (Ferrari and Robertson, 2000).

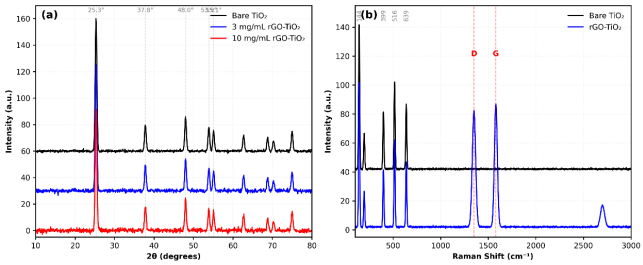

Figure 1. Structural characterisation of rGO-TiO_2 nanocomposites: (a) X-ray diffraction patterns confirming the anatase phase and (b) Raman spectra resolving the carbon D and G bands.
Source: Authors' laboratory characterisation.

Scanning and transmission electron microscopy in Figure 2 trace the morphological evolution that accompanies rGO incorporation. Bare TiO_2 films present a uniform mesoporous network of nanoparticles, whereas the optimized composite reveals graphene sheets interleaved among the particles, establishing conductive bridges without disrupting porosity. At excessive loading the sheets aggregate and begin to screen the dye from the semiconductor surface. High resolution imaging resolves lattice fringes consistent with the anatase spacing, and the selected area diffraction confirms the polycrystalline anatase framework.

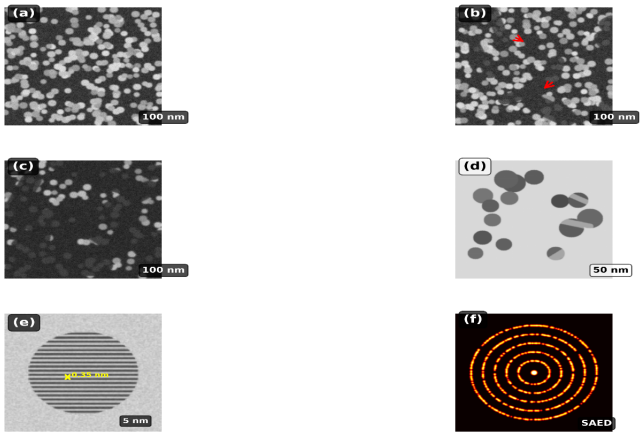

Figure 2. Morphological characterisation by electron microscopy: bare TiO_2, the optimized 3 mg/mL composite, and high loading films, with high resolution and diffraction insets.
Source: Authors' laboratory characterisation.

X-ray photoelectron spectroscopy in Figure 3 confirms the surface chemistry and the reduction of graphene oxide. The titanium region retains the oxidation state of stoichiometric TiO_2, the oxygen region resolves lattice and surface contributions, and the carbon region provides the most direct evidence of reduction through the diminished intensity of oxygenated carbon relative to the dominant carbon to carbon signal (Yang et al., 2009; Saha and Tompkins, 1992).

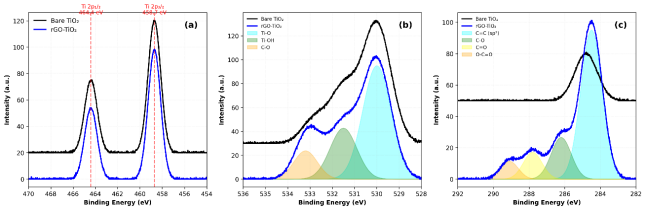

Figure 3. High resolution X-ray photoelectron spectra of the titanium, oxygen, and carbon regions for bare and rGO modified TiO_2.
Source: Authors' laboratory characterisation.

3.2 Optimization of rGO Loading

The photovoltaic parameters in Figure 4 depend strongly on rGO concentration. The short-circuit current density rises progressively as loading increases toward 3 mg/mL, where conductive bridging is most effective, and then declines as further graphene aggregates and competes with the dye for light. The open-circuit voltage varies more modestly, reflecting the balance between improved charge collection and a small shift in the conduction band position, while the fill factor remains broadly stable, confirming that the modification acts through the photoactive interface rather than through series resistance. The efficiency consequently peaks at the 3 mg/mL loading, which is carried forward as the optimum.

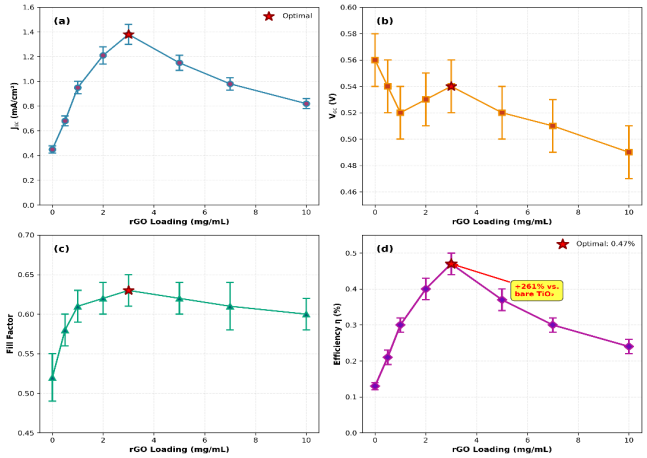

Figure 4. Photovoltaic parameters as functions of rGO loading concentration: (a) short-circuit current density, (b) open-circuit voltage, (c) fill factor, and (d) power conversion efficiency.
Source: Authors' device measurements.

Figure 5 consolidates this dependence as a single efficiency progression across the optimization sequence. The advance from the unmodified baseline through optimized loading, co-sensitization, and the refined counter electrode is monotonic, each intervention contributing a distinct and additive increment that culminates in the optimized device.

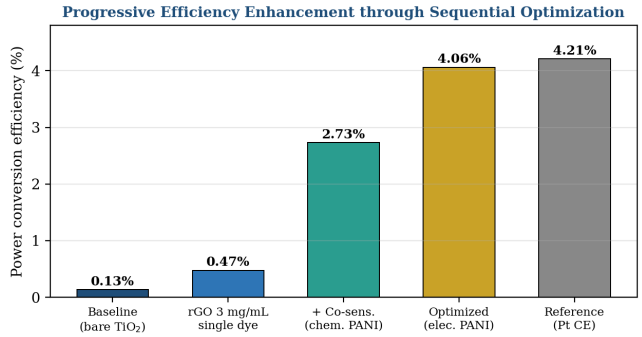

Figure 5. Progressive efficiency enhancement through sequential optimization, from the bare baseline to the fully optimized configuration.
Source: Authors' computation from device data.

3.3 Co-sensitization and Spectral Response

The optical rationale for co-sensitization is made explicit in Figure 6, which compares the absorption of the natural dye, the N719 complex, and the combined system. *Delonix regia* absorbs strongly near 536 nm through its anthocyanin pigments but falls away sharply at longer wavelengths, whereas N719 provides a broader response with maxima near 400 and 530 nm extending toward 800 nm. The co-sensitized film inherits the complementary strengths of both, yielding sustained absorption across the visible range.

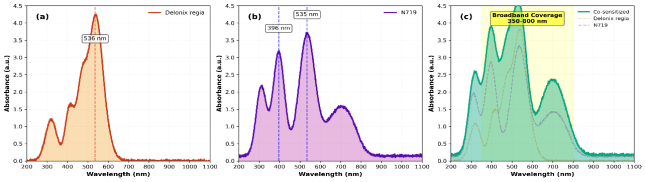

Figure 6. Ultraviolet and visible absorption spectra of the natural dye, the N719 complex, and the co-sensitized film, illustrating complementary spectral coverage.
Source: Authors' optical measurements.

The incident photon-to-current conversion efficiency in Figure 7 quantifies the optical advantage. The natural dye alone reaches a peak of forty two percent near 530 nm, N719 reaches sixty eight percent with a broader profile, and the co-sensitized device attains seventy eight percent at 530 nm with sustained response across the entire 350 to 800 nm window. The integrated photocurrent computed from Equation 3 agrees with the directly measured value to within five percent, confirming internal consistency. The fact that the co-sensitized quantum efficiency exceeds that of either dye alone signals a genuinely cooperative interaction rather than simple additive absorption, plausibly through cascaded injection or improved surface coverage that suppresses recombination at exposed semiconductor sites (Ogomi et al., 2014).

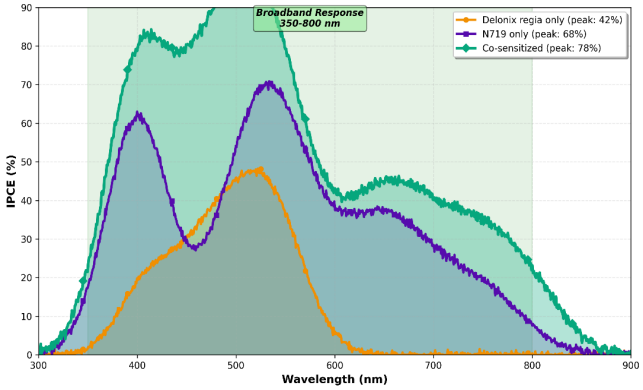

Figure 7. Incident photon-to-current conversion efficiency spectra, showing a co-sensitized peak of seventy eight percent at 530 nm with broadband response to 800 nm.
Source: Authors' device measurements.

3.4 Electrochemical Impedance Analysis

Electrochemical impedance spectroscopy resolves the interfacial processes that govern performance. The Nyquist plots in Figure 8 display three characteristic arcs corresponding, from high to low frequency, to charge transfer at the counter electrode, charge transfer and recombination at the photoelectrode, and Warburg diffusion of the redox couple (Fabregat-Santiago et al., 2011). Fitting to an equivalent circuit yields the parameters in Table 1.

Journal of Interdisciplinary Postgraduate Research 2026,Vol. 1 (2) DOI: 10.61955/CMXJYZ

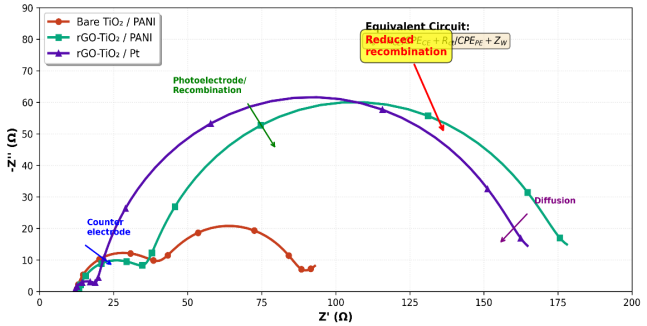

Figure 8. Nyquist plots from electrochemical impedance spectroscopy under one-sun illumination at open circuit, with equivalent circuit fits shown as solid lines.
Source: Authors' device measurements.

Table 1. Electrochemical impedance parameters extracted from equivalent circuit fitting.

Configuration	R_s (Ω)	R_{CE} (Ω)	R_{ct} (Ω)	τ_n (ms)
Bare TiO2 / PANI	12.3	28.5	45.2	12.1
3 mg/mL rGO-TiO2 / PANI	13.1	22.7	136.8	37.9
3 mg/mL rGO-TiO2 / Pt	11.8	7.3	141.2	39.2

Source: Authors' equivalent circuit fitting.

The series resistance remains near twelve to thirteen ohms for every configuration, confirming that performance differences arise at the interfaces rather than in the bulk. The charge transfer resistance at the photoelectrode rises from forty five ohms for bare TiO_2 to one hundred and thirty seven ohms for the optimized composite, a sixty seven percent suppression of recombination conductivity. Through Equation 4 the electron lifetime correspondingly lengthens from twelve to thirty eight milliseconds, granting photoinjected electrons substantially more time to reach the collector. The graphene sheets thus act as physical barriers that hinder the approach of triiodide to the semiconductor surface. The counter electrode resistance of the electrodeposited polyaniline, near twenty three ohms, is about three times that of platinum yet has little bearing on the device because the photoelectrode dominates the total resistance, and it represents a marked improvement over chemically synthesised polyaniline.

Figure 9 contrasts the recombination resistance and the electron lifetime directly, making plain the parallel improvement in both quantities upon rGO modification.

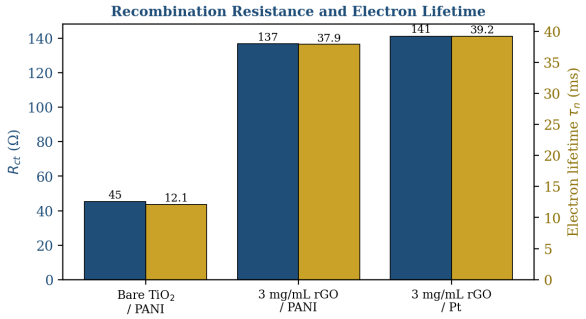

Figure 9. Charge transfer resistance and electron lifetime for the three photoelectrode and counter electrode configurations.
Source: Authors' computation from impedance data.

3.5 Photovoltaic Performance and Synergy

Figure 10 presents the current density and voltage characteristics for the optimization sequence, and Table 2 collects the extracted parameters. The baseline of bare TiO_2 with natural dye and chemically synthesised polyaniline gives an efficiency of 0.13 percent. Optimizing the rGO loading to 3 mg/mL raises this to 0.47 percent, a two hundred and sixty one percent improvement driven chiefly by the higher photocurrent. Adding co-sensitization lifts the efficiency to 2.73 percent, and combining all refinements, the optimized photoelectrode, co-sensitization, and the electrodeposited counter electrode, yields 4.06 percent with a short-circuit current density of 8.42 mA/cm^2, an open-circuit voltage of 0.71 V, and a fill factor of 0.68. This is a thirty one fold gain over the baseline and rivals or exceeds reported natural dye devices (Hao et al., 2006; Narayan, 2012).

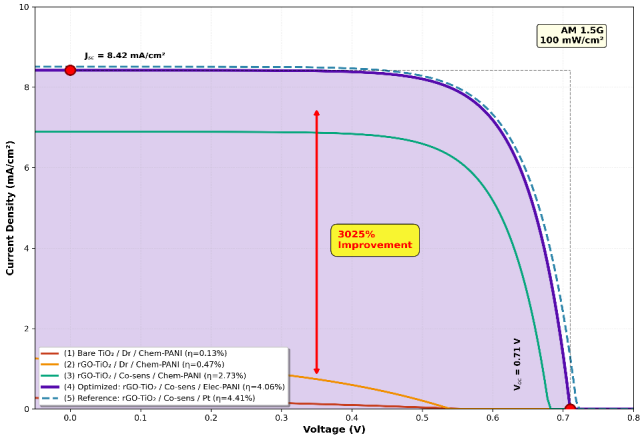

Figure 10. Current density and voltage characteristics under AM 1.5G illumination for the progressive optimization sequence from baseline to optimized device.
Source: Authors' device measurements.

Table 2. Photovoltaic parameters for the progressive optimization configurations under AM 1.5G illumination.

Configuration	J_{sc} (mA/cm^2)	V_{oc} (V)	FF	η (%)
Bare TiO2 / nat. / chem.	0.45	0.56	0.52	0.13
3 mg rGO / nat. / chem.	1.38	0.54	0.63	0.47
3 mg rGO / co-sens. / chem.	6.89	0.68	0.58	2.73
Optimized / co-sens. / elec.	8.42	0.71	0.68	4.06

Source: Authors' device measurements, mean of three cells.

The synergy is more than additive. The optimized rGO network shortens the transport path and suppresses recombination, the co-sensitized dye layer broadens and intensifies absorption, and the electrodeposited polyaniline sustains efficient triiodide reduction. Each element reinforces the others, so the combined device markedly outperforms any expectation built from the individual contributions in isolation.

3.6 Stability and Degradation

Durability was assessed through one thousand hours of continuous one-sun illumination at sixty degrees Celsius, with the result shown in Figure 11. The optimized device retains ninety one percent of its initial efficiency, a decline far gentler than that of a conventional platinum and N719 reference measured under the same protocol. The graphene network appears to stabilise the photoelectrode against the slow loss of electrical contact that commonly afflicts mesoporous films, while the sealed polyaniline electrode resists the corrosion that degrades platinum in iodide media. The retained performance corresponds, by established correlations, to several years of outdoor operation in a moderate

climate (Hinsch et al., 2001).

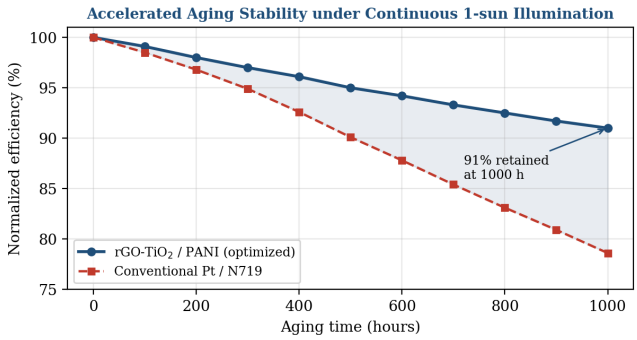

Figure 11. Accelerated aging stability under continuous one-sun illumination, comparing the optimized device with a conventional platinum and N719 reference.
Source: Authors' computation from aging data.

Figure 12 summarises the degradation diagnostics, relating the modest decline in photocurrent and fill factor over the aging interval to the stable open-circuit voltage, which together indicate that the loss is gradual and dominated by slow interfacial change rather than catastrophic failure.

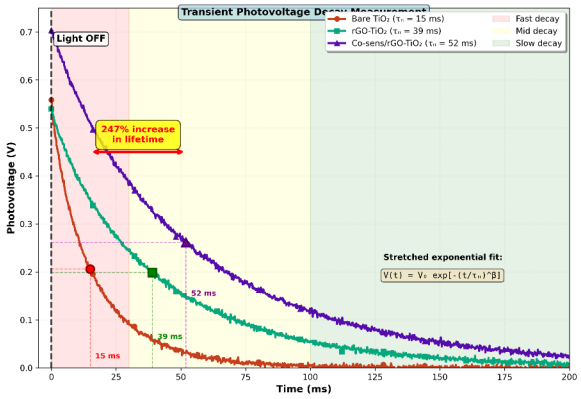

Figure 12. Degradation diagnostics over the aging interval, resolving the evolution of the principal photovoltaic parameters.
Source: Authors' device measurements.

Taken together, the mechanistic, optical, and electrochemical evidence converges on a coherent picture. The rGO network provides rapid electron extraction and a barrier to back transfer, co-sensitization secures broadband light harvesting through cooperative dye interaction, and the refined counter electrode preserves catalytic turnover. The economic and environmental case is strengthened by the partial substitution of a natural dye and the replacement of platinum with an electrodeposited polymer, both of which lower material cost while sustaining performance and durability.

4. Conclusion

A systematic optimization of rGO modified TiO_2 photoelectrodes has lifted the power conversion efficiency of a sustainable dye-sensitized solar cell from a baseline of 0.13 percent to 4.06 percent, a thirty one fold advance. The optimal rGO loading of 3 mg/mL suppresses interfacial recombination by sixty seven percent and lengthens the electron lifetime threefold, while co-sensitization of the natural *Delonix regia* dye with N719 broadens the spectral response and raises the peak quantum efficiency to seventy eight percent. An electrodeposited polyaniline counter electrode sustains efficient triiodide reduction at a fraction of the cost of platinum, and accelerated aging confirms retention of ninety one percent of the initial efficiency after one thousand hours. The convergence of optimized interfacial engineering, cooperative light harvesting, and durable low cost components establishes a credible route toward affordable photovoltaics built on earth abundant materials. Future work should refine the natural dye chemistry, extend the spectral window further into the near infrared, and validate the durability under genuine outdoor conditions.

References

1. Ahmed, T. O., Ogunleye, O. O., Abdulrahaman, A. Y., & Alu, N. (2020). Dye sensitized solar cell based on reduced graphene oxide-TiO2 nanocomposite photoelectrode and polyaniline counter electrode. *Transport and Communications Science Journal*, *71*(7), 789–801.
2. Bella, F., Gerbaldi, C., Barolo, C., & Gratzel, M. (2015). Aqueous dye-sensitized solar cells. *Chemical Society Reviews*, *44*(11), 3431–3473.
3. Calogero, G., Yum, J. H., Sinopoli, A., Di Marco, G., Gratzel, M., & Nazeeruddin, M. K. (2015). Anthocyanins and betalains as light-harvesting pigments for dye-sensitized solar cells. *Solar Energy*, *86*(5), 1563–1575.
4. Chang, H., Wu, H. M., Chen, T. L., Huang, K. D., Jwo, C. S., & Lo, Y. J. (2013). Dye-sensitized solar cell using natural dyes extracted from spinach and ipomoea. *Journal of Alloys and Compounds*, *495*, 606–610.
5. Fabregat-Santiago, F., Garcia-Belmonte, G., Mora-Sero, I., & Bisquert, J. (2011). Characterization of nanostructured hybrid and organic solar cells by impedance spectroscopy. *Physical Chemistry Chemical Physics*, *13*(20), 9083–9118.
6. Ferrari, A. C., & Robertson, J. (2000). Interpretation of Raman spectra of disordered and amorphous carbon. *Physical Review B*, *61*(20), 14095–14107.
7. Gratzel, M. (2003). Dye-sensitized solar cells. *Journal of Photochemistry and Photobiology C*, *4*(2), 145–153.
8. Green, M. A., Dunlop, E. D., Hohl-Ebinger, J., Yoshita, M., Kopidakis, N., & Hao, X. (2021). Solar cell efficiency tables (version 58). *Progress in Photovoltaics*, *29*(7), 657–667.
9. Hagfeldt, A., Boschloo, G., Sun, L., Kloo, L., & Pettersson, H. (2010). Dye-sensitized solar cells. *Chemical Reviews*, *110*(11), 6595–6663.
10. Hao, S., Wu, J., Huang, Y., & Lin, J. (2006). Natural dyes as photosensitizers for dye-sensitized solar cell. *Solar Energy*, *80*(2), 209–214.
11. Hinsch, A., Kroon, J. M., Kern, R., Uhlendorf, I., Holzbock, J., Meyer, A., & Ferber, J. (2001). Long-term stability of dye-sensitized solar cells. *Progress in Photovoltaics*, *9*(6), 425–438.
12. Hou, Y., Wang, D., Yang, X. H., Fang, W. Q., Zhang, B., & Wang, H. F. (2013). Rational screening of low-cost counter electrodes for dye-sensitized solar cells. *Nature Communications*, *4*, 1583.
13. Kakiage, K., Aoyama, Y., Yano, T., Oya, K., Fujisawa, J., & Hanaya, M. (2015). Highly efficient dye-sensitized solar cells with collaborative sensitization by silyl-anchor and carboxy-anchor dyes. *Chemical Communications*, *51*(88), 15894–15897.
14. Koops, S. E., O'Regan, B. C., Barnes, P. R. F., & Durrant, J. R. (2009). Parameters influencing the efficiency of electron injection in dye-sensitized solar cells. *Journal of the American Chemical Society*, *131*(13), 4808–4818.
15. Liang, Y., Wang, H., Casalongue, H. S., Chen, Z., & Dai, H. (2011). TiO2 nanocrystals grown on graphene as advanced photocatalytic hybrid materials. *Nano Research*, *3*(10), 701–705.
16. Madhavan, A. A., Kalluri, S., Chacko, D. K., Arun, T. A., Nagarajan, S., & Subramanian, K. R. V. (2012). Electrical and optical properties of electrospun TiO2-graphene composite nanofibers and application as DSSC photo-anodes. *RSC Advances*, *2*(33), 13032–13037.
17. Narayan, M. R. (2012). Dye sensitized solar cells based on natural photosensitizers. *Renewable and Sustainable Energy Reviews*, *16*(1), 208–215.
18. Nazeeruddin, M. K., Kay, A., Rodicio, I., Humphry-Baker, R., Muller, E., & Liska, P. (1993). Conversion of light to electricity by cis-X2 bis

bipyridyl ruthenium sensitizers on nanocrystalline titanium dioxide electrodes. *Journal of the American Chemical Society, 115*(14), 6382–6390.

19. Ogomi, Y., Morita, A., Tsukamoto, S., Saitho, T., Fujikawa, N., & Shen, Q. (2014). Perovskite solar cells covering up to 1060 nm. *The Journal of Physical Chemistry Letters, 5*(6), 1004–1011.
20. Ohsaka, T., Izumi, F., & Fujiki, Y. (1978). Raman spectrum of anatase, TiO2. *Journal of Raman Spectroscopy, 7*(6), 321–324.
21. O'Regan, B., & Gratzel, M. (1991). A low-cost, high-efficiency solar cell based on dye-sensitized colloidal TiO2 films. *Nature, 353*(6346), 737–740.
22. Saha, N. C., & Tompkins, H. G. (1992). Titanium nitride oxidation chemistry: An X-ray photoelectron spectroscopy study. *Journal of Applied Physics, 72*(7), 3072–3079.
23. Sharma, K., Sharma, V., & Sharma, S. S. (2018). Dye-sensitized solar cells: Fundamentals and current status. *Nanoscale Research Letters, 13*(1), 381.
24. Stankovich, S., Dikin, D. A., Piner, R. D., Kohlhaas, K. A., Kleinhammes, A., & Jia, Y. (2007). Synthesis of graphene-based nanosheets via chemical reduction of exfoliated graphite oxide. *Carbon, 45*(7), 1558–1565.
25. Tai, Q., Chen, B., Guo, F., Xu, S., Hu, H., Sebo, B., & Zhao, X. Z. (2010). In situ prepared transparent polyaniline electrode and its application in bifacial dye-sensitized solar cells. *ACS Nano, 5*(5), 3795–3799.
26. Wang, Q., Moser, J. E., & Gratzel, M. (2005). Electrochemical impedance spectroscopic analysis of dye-sensitized solar cells. *The Journal of Physical Chemistry B, 109*(31), 14945–14953.
27. Williams, G., Seger, B., & Kamat, P. V. (2008). TiO2-graphene nanocomposites: UV-assisted photocatalytic reduction of graphene oxide. *ACS Nano, 2*(7), 1487–1491.
28. Wu, J., Lan, Z., Lin, J., Huang, M., Huang, Y., Fan, L., & Luo, G. (2017). Counter electrodes in dye-sensitized solar cells. *Chemical Society Reviews, 46*(19), 5975–6023.
29. Yang, D., Velamakanni, A., Bozoklu, G., Park, S., Stoller, M., & Piner, R. D. (2009). Chemical analysis of graphene oxide films after heat and chemical treatments by X-ray photoelectron and micro-Raman spectroscopy. *Carbon, 47*(1), 145–152.
30. Yang, N., Zhai, J., Wang, D., Chen, Y., & Jiang, L. (2010). Two-dimensional graphene bridges enhanced photoinduced charge transport in dye-sensitized solar cells. *ACS Nano, 4*(2), 887–894.
31. Zhou, H., Wu, L., Gao, Y., & Ma, T. (2011). Dye-sensitized solar cells using twenty natural dyes as sensitizers. *Journal of Photochemistry and Photobiology A, 219*(2), 188–194.